Chinese Chemical Letters 37 (2026) 111435

Contents lists available at ScienceDirect

Chinese Chemical Letters

journal homepage: www.elsevier.com/locate/cclet

Nano-confined electrolyte enabled by pre-desolvation strategy for efficient lithium-metal batteries

Danni Zhang[a], Yan Xu[a], Shibin Zhang[a], Lishun Bai[a], Yue Liu[a], Kuhang Liu[a], Ying He[a], Feiyan Yu[a], Sijie Li[b,*], Zhi Chang[a,*]

[a] Key Laboratory of Electronic Packaging and Advanced Functional Materials of Hunan Province, School of Materials Science and Engineering, Central South University, Changsha 410083, China
[b] College of Chemistry and Chemical Engineering, Central South University, Changsha 410083, China

ARTICLE INFO

Article history:
Received 23 May 2025
Revised 7 June 2025
Accepted 10 June 2025
Available online 10 June 2025

Keywords:
Lithium-metal battery
Metal-organic frameworks
Dendrite-free lithium
Electrolyte
Anode interface

ABSTRACT

Lithium-metal batteries (LMBs) are promising next-generation high-energy-density systems due to lithium's high theoretical capacity. However, while ester-based electrolytes support high-voltage cathodes, their poor compatibility with lithium metal hinders progress. In this study, a porous material with sub-nanochannels was constructed on lithium metal, inducing a pre-desolvation process that promotes a highly aggregative nano-confined electrolyte. This design mitigates solvent-lithium reactivity, enabling dendrite-free deposition and a stable LiF-rich solid electrolyte interphase (SEI). As a result, NCM-811//Li ($LiNi_{0.8}Co_{0.1}Mn_{0.1}O_2$//Li) cell achieved exceptional cycling stability (89.2% capacity retention after >400 cycles). This strategy provides a viable pathway for advanced high-energy-density batteries.

© 2026 Published by Elsevier B.V. on behalf of Chinese Chemical Society and Institute of Materia Medica, Chinese Academy of Medical Sciences.

Modern society demands high-energy-density batteries [1–3]. Lithium-metal batteries (LMBs), employing lithium metal anodes paired with high-voltage cathodes, offer a promising solution to overcome the capacity limitations of graphite anodes in conventional lithium-ion batteries [4–7]. However, traditional ester-based electrolytes face inherent challenges [8], including: Sluggish Li^+ desolvation, unstable SEI formation, uncontrolled lithium dendrite growth, and low Coulombic efficiency [9,10]. These issues cause rapid capacity fade, shortened lifespan, and safety risks (Fig. 1a) [11,12]. Crucially, these problems stem from incompatible reactions between electrolyte solvents (released during Li^+ desolvation) and reactive lithium metal [13].

Various electrolyte strategies have been developed to address these challenges in LMBs [14,15]. Highly concentrated electrolytes and localized highly concentrated electrolytes (HCEs and LHCEs) show particular promise by modifying Li^+ solvation structures to reduce free solvents and side reactions [14,16–20]. However, HCEs face critical limitations: They require expensive lithium salts in large quantities [21,22], increasing costs and compromising scalability. Moreover, their high viscosity impedes Li^+ transport [23], degrading rate capability and efficiency [24]. These drawbacks underscore the need for alternative approaches that overcome Li-metal incompatibility without introducing new trade-offs.

To mitigate side reactions between lithium metal and desolvated solvent molecules, we propose an electrically insulating porous matrix with sub-nano channels. Unlike HCEs that require excess lithium salts, our approach selectively removes solvent molecules from solvated Li^+ [25]. The matrix's sub-nano pores (smaller than solvated ions) force desolvation before ions reach the electrode, preventing solvent-lithium interactions [26]. This creates a nano-confined electrolyte rich in contacted ion-pairs and aggregative (CIPs and AGG) solvation modes, enhancing Li^+ transport and electrolyte stability (Fig. 1b). The resulting benefits include: (1) Accelerated Li^+ desolvation, (2) suppressed dendrite growth, and (3) stable SEI formation—collectively improving Coulombic efficiency and safety. This strategy overcomes ester electrolyte limitations while maintaining compatibility with high-voltage cathodes, enabling practical high-energy-density batteries.

This study constructed an electrically insulating ZIF-61 porous matrix with sub-nano channels on lithium metal, creating a unique nano-confined electrolyte. ZIF-61's narrow pores enabled Li^+ pre-desolvation and promoted highly aggregative electrolyte formation, yielding three key advantages: (1) Extended electrochemical stability window, (2) enhanced lithium compatibility, and (3) improved safety (non-flammable). These properties enabled dendrite-free deposition, reduced electrolyte decomposition, and formed a robust LiF-rich SEI. The resulting NCM-811//Li battery achieved excep-

* Corresponding authors.
E-mail addresses: li.sijie@csu.edu.cn (S. Li), ZhiChang@csu.edu.cn (Z. Chang).

https://doi.org/10.1016/j.cclet.2025.111435
1001-8417/© 2026 Published by Elsevier B.V. on behalf of Chinese Chemical Society and Institute of Materia Medica, Chinese Academy of Medical Sciences.

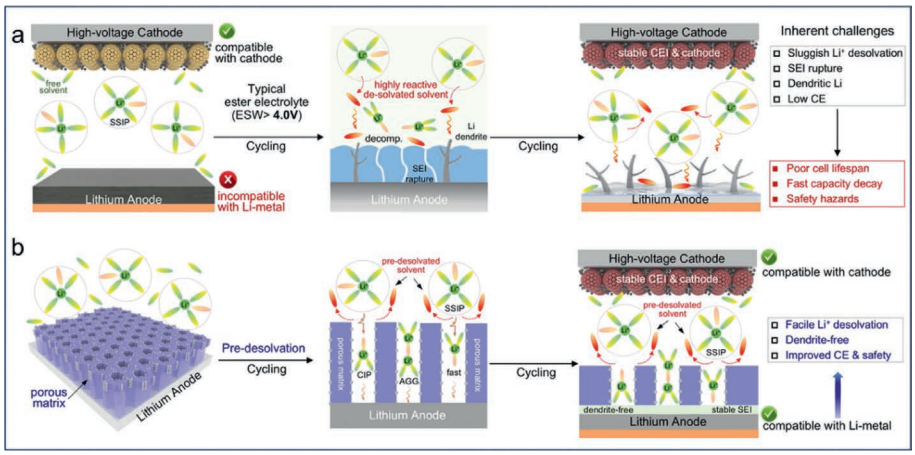


Fig. 1. Role of porous matrix coating in enabling Li^+ pre-desolvation for high-voltage LMBs. (a) Limitations of conventional ester electrolytes. (b) Mechanism and benefits of Li^+ pre-desolvation in matrix-coated batteries.

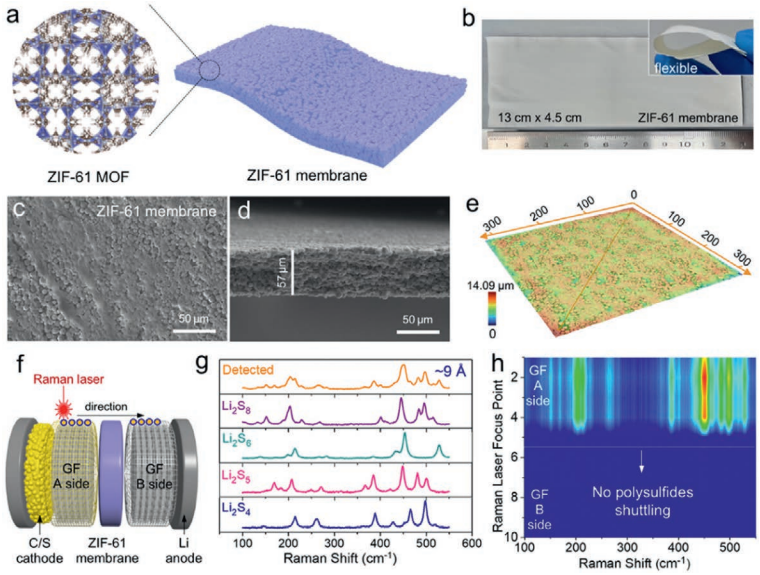


Fig. 2. Preparation and the corresponding physical characterization of the prepared ZIF-61 membrane. (a) Schematic of the ZIF-61 MOF based self-supporting membrane. (b) Digital photo of the flexible prepared ZIF-61 membrane. (c) Top-view and (d) side-view SEM image of ZIF-61 membrane. (e) 3D reconstructed Confocal laser scanning microscopy (CLSM) image of ZIF-61 membrane. (f) Schematic illustration of the Raman measurement and lithium-sulfur battery architecture employed for the verification of the suppression of polysulfides by using ZIF-61 membrane as separator (g) Raman spectra of various lithium polysulfide and the Raman spectrum detected from (f). (h) The corresponding color mapping reflecting lithium polysulfide distribution of Raman information collected from (f).

tional cycling stability (89.2 % capacity retention after >400 cycles) and rate capability. This approach provides a practical pathway for high-energy-density battery development.

We selected ZIF-61, a Zn-based MOF with pore channels narrower than solvated Li^+, to validate our strategy. Synthesized as a white polyhedral powder (Figs. S1 and S2 in Supporting information), ZIF-61 was processed into a flexible 13×4.5 cm^2 membrane (Figs. 2a and b) while maintaining structural integrity (Fig. S3 in Supporting information). SEM revealed a dense, uniform morphology with PTFE-bridged particles (Figs. 2c and d, Fig. S4 in Supporting information) and a 57-μm thickness. Confocal laser scanning microscopy (CLSM) confirmed low surface roughness (Fig. 2e and Fig. S5 in Supporting information), while contact angle tests showed slightly higher wettability than PP separators in $LiPF_6$-EC/DEC electrolyte (Fig. S6 in Supporting information).

To verify the densification and effectiveness of the ZIF-61 membrane, a lithium-sulfur battery equipped with the as-prepared ZIF-61 membrane was assembled. The distribution of lithium polysulfide on two sides of the membrane was then analyzed (Fig. 2f). The detection result, represented by the orange line in Fig. 2g, revealed characteristic peaks corresponding to various lithium polysulfides species (Li_2S_x, $x = 4$, 5, 6, 8), with molecular size around 9 Å [27–29]. In this case, the Raman spectroscopy was performed by scanning from side A to side B of the glass fiber (GF). Clearly, the analysis showed a significant accumulation of lithium polysulfides on side A of the GF, whereas the B side of GF contained almost no lithium polysulfide (Fig. 2h and Fig. S8 in Supporting information). In sharp contrast, a similar test conducted on the PP separator revealed the presence of polysulfides on both sides, confirming its inability to suppress polysulfide shuttling (Fig. S7 in Supporting information). The permeation experiments demonstrate that lithium polysulfide molecules (~8–9 Å in size) cannot penetrate the ZIF-61 membrane, confirming its effectiveness in blocking small-molecule diffusion. Given the similar size of solvated lithium ions (~8 Å), transport through interparticle voids is unlikely. Thus, solvated Li^+ ions can only permeate through the sub-nanochannels of ZIF-61. Under an applied electric field, solvated lithium ions must partially de-solvate (shed solvent molecules from their sol-

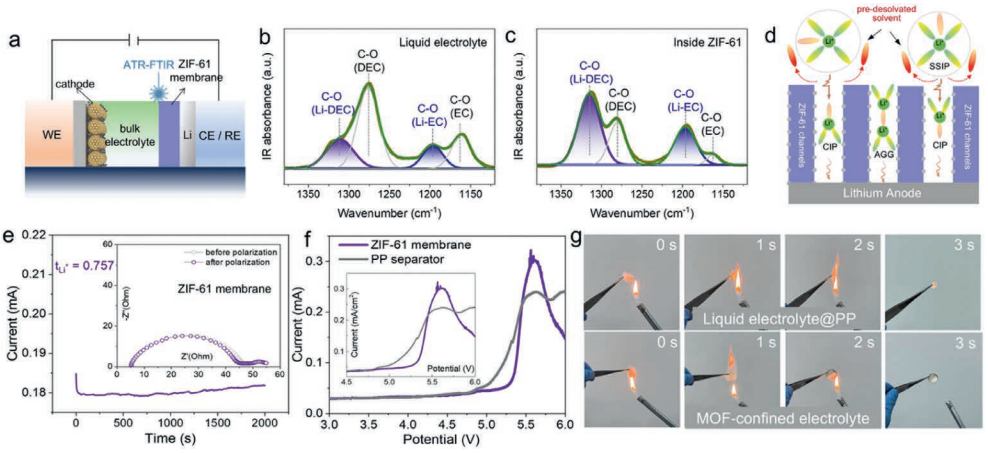


Fig. 3. Physicochemical properties of the prepared ZIF-61 based nano-confined electrolyte. (a) Schematic illustration of the Attenuated total reflectance Fourier transforms infrared (ATR-FTIR) spectroscopy measurement used for study the configuration of electrolyte. FTIR spectra of (b) typical ester-based liquid electrolyte and (c) electrolyte inside ZIF-61 sub-nanochannels. (d) Schematically illustration of the electrolyte configuration confined within the ZIF-61 channels (namely the ZIF-61 based nano-confined electrolyte). (e) Polarization curves and the electrochemical impedance spectra (inset) of the ZIF-61 based nano-confined electrolyte. (f) Linear sweep voltammetry (LSV) curve of the ZIF-61 based nano-confined electrolyte. (g) Digital photos of flammability tests of typical ester-based liquid electrolyte impregnated PP separator and the as-prepared ZIF-61 based nano-confined electrolyte.

vation shells) before entering the ZIF-61 channels. Consequently, Li^+ transport occurs exclusively through the ZIF-61 nanochannels (Fig. S9 and Table S1 in Supporting information).

After the ZIF-61 membrane was closely pressed onto the surface of the lithium anode, NCM-811//Li half-cells were assembled by using typical 1 mol/L $LiPF_6$-EC/DEC as electrolyte. Following twenty charge/discharge cycles (during which the electrolyte was subjected to an external electric field within the sub-nano channels of ZIF-61), the cycled membrane (prepared nano-confined electrolyte) was analyzed using Attenuated Toal Reflection-Fourier Transform Infrared (ATR-FTIR) spectroscopy (Fig. 3a) to investigate the information of the electrolyte confined within the MOF channels (Fig. 3c). For comparison, the correlation spectra of typical liquid electrolytes were tested (Fig. 3b).

Apparently, the wavenumber corresponding to C–O bonds in EC and DEC (gray lines) and their Li^+-bonded counterparts (blue and purple lines) were observed in the range of 1120 and 1380 cm^{-1} [30,31]. For liquid electrolyte, the solvated EC and DEC were the dominant configuration [32]. In stark contrast, the opposite result was observed, where the Li^+-bonded configuration was predominantly present inside the ZIF-61 membrane. Notably, the nanoconfined electrolyte within ZIF-61 exhibits significantly greater ion aggregation compared to both conventional diluent liquid electrolyte (Fig. 3b) and saturated liquid electrolyte (Fig. S10 in Supporting information). These results indicated significantly enhanced lithium-solvent interactions and a more aggregated electrolyte conformation within the ZIF-61 channels (Fig. 3d).

To further assess the stability of the ZIF-61 based nano-confined electrolyte during cycling, a Li//Li symmetric cell was assembled and cycled for various cycles, and the disassembled ZIF-61 based nano-confined electrolyte was examined using X-ray diffraction (XRD). Clearly, the characteristic peaks of the cycled ZIF-61 based nano-confined electrolyte matched those of the pristine membrane, confirming the remarkable stability of the ZIF-61 membrane during charge/discharge processes (Fig. S11 in Supporting information). Collectively, these findings demonstrated that the ZIF-61 membrane not only possessed an aggregative electrolyte inside its sub-nano channels, but also enhanced lithium-ion transport and improved battery safety.

Further investigations into the physicochemical properties of the nano-confined electrolyte revealed a high lithium-ion transport number of 0.757 (Fig. 3e), significantly higher than that of conventional liquid electrolyte [33]. The apparent high Li^+ transference number of the nano-confined electrolyte was thought closely related to the Li^+ pre-desolvation process. When passing through the channel, the small diameter of the ZIF-61 will restrict anion conduction due to the comparatively larger dimensions of anions than Li^+. According to the fundamental principle of charge conservation ($t_+ + t_- = 1$), this suppressed anion transport (due to its relative larger size compared with lithium-ion) inherently elevates the lithium-ion transference number (t_+) (Fig. 3e). The apparently suppressed anion transport further supports our conjecture that the lithium-ion underwent pre-desolvation before entering the channels of ZIF-61. The linear sweep voltammetry (LSV) test demonstrated that the electrochemical stabilization window (ESW) of the ZIF-61 based nano-confined electrolyte was exceeded 5.25 V, which was apparently much wider than that of traditional liquid electrolyte (Fig. 3f and Fig. S12 in Supporting information), for both diluent and saturated electrolytes). Potentiostatic Intermittent Titration Technique floating (PITT floating) test and of typical electrolyte and the prepared ZIF-61 based nano-confined electrolyte (Fig. S13 in Supporting information). Obviously, after cycled for 400 cycles, the ZIF-61 based nano-confined electrolyte still exhibit excellent stability even under high voltage of 5.2 V. Additionally, the ZIF-61 based nano-confined electrolyte exhibited excellent flame retardancy. While the typical liquid electrolyte (simply impregnated into a PP separator) burned completely within only 2 s under ignition (Fig. 3g), ZIF-61 based nano-confined electrolyte maintained its morphological integrity under continuous flame exposure, highlighting its superior thermal stability.

The compatibility between lithium metal and ZIF-61 based nano-confined electrolyte was evaluated by Li plating/stripping tests using Li//Li symmetric batteries assembled with the as-prepared ZIF-61 based nano-confined electrolyte. As shown in Fig. 4a, Li//Li cell with ZIF-61 based nano-confined electrolyte exhibited relatively low and stable overpotentials of about 50 mV, maintaining stable operation for over 1000 h under the current density of 0.5 mA/cm^2 at room temperature (purple curve). Notably, the overpotentials tend to gradually decreased during the initial 100 h (from 74 mV to 46 mV), likely due to the enhanced interfacial conformability of lithium metal after cycling, which suppressed lithium dendrites growth and inhomogeneous lithium deposition. In stark contrast, Li//Li symmetric cell (grey curve) demonstrated a sharp increase in overpotential, exceeding 400 mV

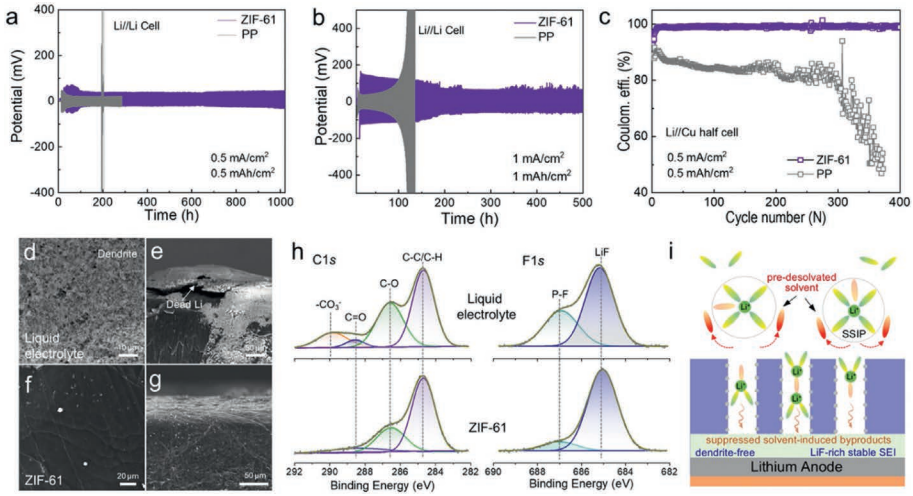


Fig. 4. Improved compatibility between lithium metal and ZIF-61 based nano-confined electrolyte. Electrochemical performance of Li//Li symmetrical cells assembled with PP separator/typical ester-based electrolyte and ZIF-61 based nano-confined electrolyte at condition of (a) 0.5 mA/cm^2, 0.5 mAh/cm^2, and (b) at 1 mA/cm^2, 1 mAh/cm^2. (c) Coulombic efficiency of Li//Cu half-cells used PP separator/typical ester-based electrolyte and ZIF-61 based nano-confined electrolyte at condition of 0.5 mA/cm^2, 0.5 mAh/cm^2. SEM images for the cycled Li-metals harvested from cell used (d, e) PP separator/typical ester-based electrolyte and (f, g) ZIF-61 based nano-confined electrolyte. The corresponding (h) XPS results of the two cycled Li anodes (left: C 1s; right: F 1s). (i) Schematically illustration of the function of ZIF-61 nano-confined electrolyte in promoting dendrite-free lithium metal with LiF-rich stable SEI during electrochemical cycling.

after 195 h, indicating the occurrence of short circuit likely caused by an unstable SEI and the formation of dendritic Li. Similar results could also be observed under a higher current density of 1 mA/cm^2 (Fig. 4b).

To further assess the stability of Li deposition and stripping, Li//Cu half-cells were tested at a current density of 0.5 mA/cm^2 and a capacity of 0.5 mAh/cm^2 (Fig. 4c). The Coulombic efficiency (CE) of Li//Cu half-cell assembled with typical ester electrolyte used PP separator began to fluctuate significantly on the 180 cycles, followed by a steep decay. In contrast, the CE of half-cell cycled with ZIF-61 based nano-confined electrolyte was much higher and stable, remaining 99.1 % after 400 cycles. Visual inspection of the copper electrodes from cycled Li//Cu cells revealed that the lithium surface modified by ZIF-61 based nano-confined electrolyte was smoother and more uniform compared to that with the PP separator and typical ester-based electrolyte at various current densities (Fig. S14 in Supporting information). Additionally, the corresponding SEM images confirmed that the lithium harvested from cell based on PP separator exhibited loose and porous structure with numerous dendrites, whereas the cycled lithium based on ZIF-61 based nano-confined electrolyte was flat and dense, indicating that the ZIF-61 nano-confined electrolyte promoted homogeneous deposition and stripping of lithium metals. Furthermore, the Li//Li cells cycled at 0.25 and 0.5 mA/cm^2 current densities were disassembled after 10, 25 and 50 times, respectively. It was found that the lithium cycled within typical ester-based electrolyte displayed extensive dendrites formation, and uneven cross-section, and visible by-products detached from the lithium substrate (Figs. 4d and e, Figs. S15-S18 in Supporting information). In contrast, the lithium protected by the ZIF-61 based nano-confined electrolyte exhibited a uniform surface and a dense, flat cross-section (Figs. 4f and g, Figs. S15-S18). demonstrating that the ZIF-61 based nano-confined electrolyte effectively prohibited the growth of lithium dendrites and the formation of dead Li.

Electrochemical impedance spectroscopy (EIS) of the symmetric cells was conducted to analyze the change-transfer resistance and the Li^+ diffusion (Figs. S19 and S20 in Supporting information). While the Nyquist plots of two cells appeared similar, the cell based on ZIF-61 nano-confined electrolyte exhibited lower change transfer resistance, faster ion transport, and presumably a more stable SEI. To investigate the composition of SEI, X-ray photoelectron spectroscopy (XPS) was performed on the lithium metals of symmetric cells after 10 cycles. The C 1s and F 1s XPS spectra revealed a prominent carbonate-related peak (284.7 eV) in the sample based on PP separator and typical ester-based electrolyte, resulting from electrolyte decomposition (Fig. 4h, upper panel) [34]. In contrast, the cycled Li metal harvested from cell based on ZIF-61 nano-confined electrolyte showed no such peak but a larger proportion of lithium fluoride (LiF) (Fig. 4h, lower panel), indicating significantly reduced solvent-related by-products and dendrite-free SEI dominated by LiF (Fig. 4i).

These encouraging results summarized above motivated us to explore the potential of constructing high-energy-density LMBs with the as-prepared nano-confined electrolyte. Cells incorporating a high-nickel-content cathode material $LiNi_{0.8}Co_{0.1}Mn_{0.1}O_2$ (NCM-811) paired with lithium anode were assembled for further electrochemical characterization. As shown in Figs. 5a and b, compared to NCM-811//Li batteries cycled in conventional ester-based liquid electrolyte, the batteries using ZIF-61 based nano-confined electrolyte exhibited significantly enhanced performance in terms of both cycling life and capacity. At a high cut-off voltage of 4.3 V, NCM-811//Li assembled with ZIF-61 based nano-confined electrolyte delivered a high capacity of 171.2 mAh/g and maintained at 152.8 mAh/g (89.2 % capacity retention) after 430 cycles. In sharp contrast, the NCM-811//Li cell with typical ester-based liquid electrolyte experienced a rapid capacity degradation, retaining only 41.4 mAh/g (73.1 % capacity retention) after 110 cycles (Fig. S21 in Supporting information).

In addition, the rate performance of NCM-811//Li batteries were measured by galvanostatic charge/discharge at variable rates, from 0.1 C to 2 C, within a potential window of 2.7–4.3 V *versus* Li/Li^+ (Fig. 5c). As can be seen, the cell assembled with PP separator and typical ester-based electrolyte initially delivered a discharge capacity of 220.9 mAh/g at 0.1 C, but it dropped to only 119.6 mAh/g at 2 C, retaining merely about 54 % of its initial capacity. In contrast, with the ZIF-61 membrane, the NCM-811//Li cell based on ZIF-61 nano-confined electrolyte exhibited high discharge capacities of 224.2, 212.3, 197.1, 184.2, and 167.6 mAh/g, at 0.1, 0.2, 0.5, 1, 2 C, respectively. In particular, when the current density was suddenly switched from 2 C to 1 C, the cell recov-

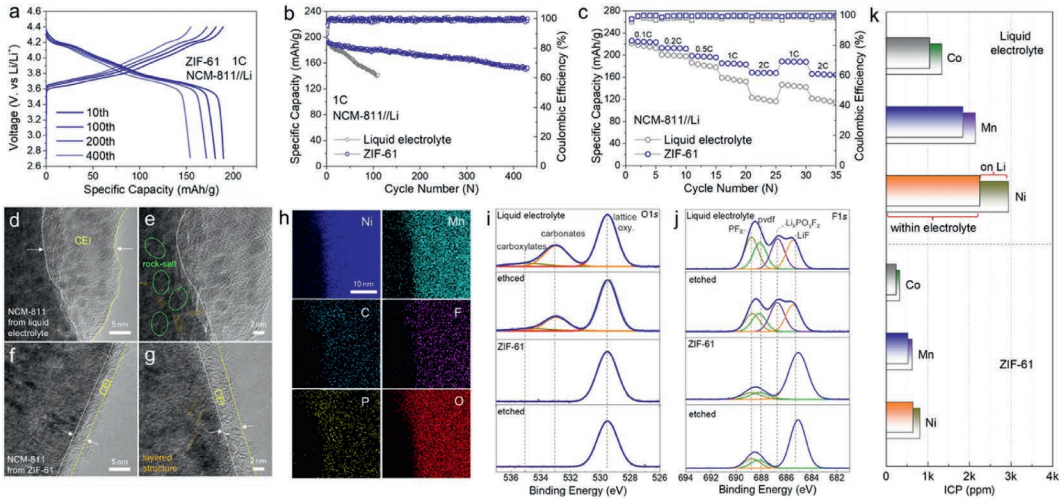


Fig. 5. Electrochemical performance of NCM-811//Li cells with ZIF-61 nano-confined electrolyte and post-cycled cathode analysis. (a) Charge/discharge curves and (b) cycling stability at 1 C. (c) Rate capability comparison: conventional *vs.* ZIF-61 electrolyte. TEM of cycled NCM-811 cathodes. (d, e) Conventional electrolyte; (f, g) ZIF-61 electrolyte. (h) EDS mapping of NCM-811 cathode (ZIF-61 system, 0.5 C after 20 cycles). Depth-resolved XPS: (i) O 1s and (j) F 1s spectra (top: conventional; bottom: ZIF-61). (k) ICP analysis of transition metal dissolution.

ered a high-reversible specific capacity of 188.0 mAh/g, indicating the excellent reversibility and stability. These results highlight the superior performance of high-voltage NCM-811//Li batteries equipped with the ZIF-61 based nano-confined electrolyte. To further investigate the effect of ZIF-61 based nano-confined electrolyte on high-voltage cathode, SEM and transmission electron microscope (TEM) analyses were conducted on the NCM-811 cathode after cycling. For the NCM-811 cathode cycled in the typical ester-based electrolyte, the cathode electrolyte interface (CEI) layer appeared uneven and irregular (Figs. 5d and e, Figs. S22-S24 in Supporting information). More critically, a disordered rock salt phase transition layer, approximately 5–20 nm thick, was clearly observed on the NCM-811 cathode surface (Fig. 5e, highlighted by green circle). The phase transition can be attributed to the solvation of lithium ions during electrochemical cycling, leading to their co-embedding into the NCM-811 structure [22,35]. In contrast, surprisingly, the NCM-811 cathode cycled in the ZIF-61 based nano-confined electrolyte exhibited a uniformly thin CEI layer (~3–4 nm), and the NCM-811 material perfectly retained its original well-layered structure without significant degradation (Figs. 5f and g, Figs. S25 and S26 in Supporting information). Energy-dispersive X-ray spectroscopy (EDS) was used to analyze the composition of the CEI layer. The EDS elemental mapping images clearly revealed that the cycled NCM-811 cathode with ZIF-61 based nano-confined electrolyte had a quite thin CEI layer with minimal solvent-related decomposition by-products (Fig. 5h, Figs. S27 and S28 in Supporting information), showing lower distribution of C, F and P). In comparison, the CEI layer formed with the conventional electrolyte contained a significant amount of decomposition byproducts (Fig. S29 in Supporting information). These results demonstrate the significant role of ZIF-61 based nano-confined electrolyte in stabilizing the cathode-electrolyte interface, minimizing detrimental side reactions and preserving the structural integrity of the NCM-811 cathode. To gain deeper insights into the surface composition of the CEI layer, etching XPS test was performed on the two cycled NCM-811 cathodes. In the O 1s XPS spectra, peaks corresponding to lattice oxygen (529.5 eV) could be found in both cycled NCM-811 cathodes [36–38].

Cycled with the controlled by ZIF-61 based nano-confined electrolyte showed a considerable higher proportion of LiF both before and after etching, confirming that the CEI layer was predominantly comprised of stable LiF. Further quantitative analysis using inductively coupled plasma (ICP) measurements was conducted to assess the dissolved transition metal ions. While substantial amounts of Ni, Co, and Mn were detected in the conventional ester-based electrolyte system (Fig. 5k, upper panel), the ZIF-61 based nano-confined electrolyte and the corresponding lithium anode exhibited only minimal dissolved transition metal ions (lower panel, <1000 ppm after 20 cycles). Therefore, the stability of the whole batteries was effectively boosted by using this novel strategy. These results demonstrate that the ZIF-61 based nano-confined electrolyte significantly enhances the stability of the entire battery system, effectively mitigating transition metal dissolution and improving the overall performance of battery.

In this study, we reported a lithium-ion pre-desolvation strategy by using electrical insulating porous ZIF-61 material with sub-nano channels to prepare a special nano-confined electrolyte. Benefits from the narrow channels, lithium-ions de-solvated parts of their solvent molecules that originally with the solvated lithium-ions, and promoted highly aggregative electrolyte inside its sub-nanochannels. This unique non-flammable nano-confined electrolyte possessed largely extended electrochemical stability window and significantly enhanced lithium compatibility. The nano-confined electrolyte significantly reduced detrimental electrolyte decomposition, enabled dendrite-free lithium-metal deposition, and facilitated the formation of a stable, LiF-dominated SEI layer, thereby enhancing the compatibility of ester-based electrolytes with lithium metal. As a result, Li//Li symmetric cells based on ZIF-61 based nano-confined electrolyte demonstrated greatly improved lifespan of >1000 h and Li//Cu half-cells also delivered a high CE of 99.1 % during 400 cycles. Moreover, high-voltage NCM-811//Li half-cells incorporating the ZIF-61 based nano-confined electrolyte exhibited a significantly improved LiF-dominated CEI layer, and demonstrated remarkable enhanced cycling stability, retaining 89.2 % of their capacity after >400 cycles. More importantly, we believe that nano-confined electrolyte based on lithium pre-desolvation will open new avenues for future energy storage technologies with high-energy-density.

CRediT authorship contribution statement

Danni Zhang: Writing – original draft, Methodology, Investigation, Data curation, Conceptualization. **Yan Xu:** Methodology, Investigation. **Shibin Zhang:** Methodology, Investigation. **Lishun**

Bai: Methodology, Investigation. **Yue Liu:** Methodology, Investigation. **Kuhang Liu:** Methodology, Investigation. **Ying He:** Methodology, Investigation. **Feiyan Yu:** Methodology, Investigation. **Sijie Li:** Methodology, Investigation. **Zhi Chang:** Writing – review & editing, Supervision, Resources, Funding acquisition, Conceptualization.

Declaration of competing interest

The authors declare that they have no known competing financial interests or personal relationships that could have appeared to influence the work reported in this paper.

Acknowledgments

This work was supported by the National Natural Science Foundation of China (Nos. 92372201, 22209208), National Key Research and Development Program of China (No. 2024YFB3814200).

Supplementary materials

Supplementary material associated with this article can be found, in the online version, at doi:10.1016/j.cclet.2025.111435.

References

[1] Y. Wu, L. Xie, H. Ming, et al., ACS Energy Lett. 5 (2020) 807–816.
[2] J. Chang, Q. Huang, Y. Gao, Z. Zheng, Adv. Mater. 33 (2021) 2004419.
[3] H. Wang, L. Zhao, H. Zhang, et al., Energy Environ. Sci. 15 (2022) 311–319.
[4] J. Zhou, C. Zhang, H. Wang, et al., Adv. Sci. 11 (2024) 2410129.
[5] J.F. Ding, Y.T. Zhang, R. Xu, et al., Green Energy Environ. 8 (2023) 1509–1530.
[6] Y. Xu, L. Gao, L. Shen, et al., Matter 3 (2020) 1685–1700.
[7] J. Liu, Y. Zhang, J. Zhou, et al., Adv. Funct. Mater. 33 (2023) 2302055.
[8] S. Kim, G. Park, S.J. Lee, et al., Adv. Mater. 35 (2023) 2206625.
[9] S. Wang, J. Shi, Z. Liu, Y. Xia, Adv. Energy Mater. 14 (2024) 2401526.
[10] B. Zhou, T. Deng, C. Yang, et al., Adv. Funct. Mater. 33 (2023) 2212005.
[11] D. Hubble, D.E. Brown, Y. Zhao, et al., Energy Environ. Sci. 15 (2022) 550–578.
[12] Y.K. Liu, C.Z. Zhao, J. Du, et al., Small 19 (2022) 2205315.
[13] Y. Jie, X. Liu, Z. Lei, et al., Angew. Chem. Int. Ed. 59 (2020) 3505–3510.
[14] W. Cai, Y. Deng, Z. Deng, et al., Adv. Energy Mater. 13 (2023) 2301396.
[15] M. Li, C. Wang, Z. Chen, K. Xu, J. Lu, Chem. Rev. 120 (2020) 6783–6819.
[16] Z. Wu, R. Li, S. Zhang, et al., Chem 9 (2023) 650–664.
[17] J. Zhang, Q. Li, Y. Zeng, et al., Energy Storage Mater. 51 (2022) 660–670.
[18] J. Wu, Z. You, M. Li, et al., Adv. Energy Mater. 15 (2025) 2403585.
[19] X. Cao, P. Gao, X. Ren, et al., Proc. Nat. Acad. Sci. U. S. A. 118 (2021) e2020357118.
[20] P. Nie, M. Liu, W. Qu, et al., Adv. Funct. Mater. 33 (2023) 2302235.
[21] Z. Chang, Y. Qiao, H. Deng, et al., Joule 4 (2020) 1776–1789.
[22] Z. Chang, H. Yang, Y. Qiao, et al., Adv. Mater. 34 (2022) 2201339.
[23] Y. He, Z. Chang, S. Wu, et al., Adv. Energy Mater. 8 (2018) 1802130.
[24] Z. Chang, H. Yang, X. Zhu, P. He, H. Zhou, Nat. Commun. 13 (2022) 1510.
[25] Y. Yamada, J. Wang, S. Ko, E. Watanabe, A. Yamada, Nat. Energy 4 (2019) 269–280.
[26] C. Niu, D. Liu, J.A. Lochala, et al., Nat. Energy 6 (2021) 723–732.
[27] Y. He, Y. Qiao, Z. Chang, Angew. Chem. Int. Ed. 58 (2019) 11774–11778.
[28] S. Lang, S.H. Yu, X. Feng, M.R. Krumov, H.D. Abruña, Nat. Commun. 13 (2022) 4811.
[29] H.L. Wu, L.A. Huff, A.A. Gewirth, ACS Appl. Mater. Interfaces 7 (2015) 1709–1719.
[30] Z. Chang, Y. Qiao, H. Yang, et al., Energy Environ. Sci. 13 (2020) 4122–4131.
[31] M. Matsui, S. Deguchi, H. Kuwata, N. Imanishi, Electrochemistry 83 (2015) 874–878.
[32] H. Tu, L. Li, Z. Wang, et al., ACS Nano 16 (2022) 16898–16908.
[33] P.S. Kim, A.Le Mong, D. Kim, J. Membrane Sci. 612 (2020) 118481.
[34] D. Li, H. Li, D. Danilov, et al., J. Power Sources 396 (2018) 444–452.
[35] Z. Zhao, B. Nian, Y. Lei, et al., Adv. Mater. 36 (2024) 2402626.
[36] J. George, A. K.E., Phys. B: Condens. Matter. 610 (2021) 412958.
[37] V. Jabbari, V. Yurkiv, M.G. Rasul, et al., Energy Storage Mater. 46 (2022) 352–365.
[38] S. Chen, Y. Xiang, G. Zheng, et al., ACS Appl. Mater. Interfaces 12 (2020) 27794–27802.